nature materials

LETTERS

https://doi.org/10.1038/s41563-018-0140-3

Quantum spin liquids unveil the genuine Mott state

A. Pustogow[1*], M. Bories[1], A. Löhle[1], R. Rösslhuber[1], E. Zhukova[2], B. Gorshunov[2], S. Tomić[3], J. A. Schlueter[4,5], R. Hübner[1,6], T. Hiramatsu[7], Y. Yoshida[7,8], G. Saito[7,9], R. Kato[10], T.-H. Lee[11], V. Dobrosavljević[11], S. Fratini[12] and M. Dressel[1]

The localization of charge carriers by electronic repulsion was suggested by Mott in the 1930s to explain the insulating state observed in supposedly metallic NiO. The Mott metal–insulator transition has been subject of intense investigations ever since[1–3]—not least for its relation to high-temperature superconductivity[4]. A detailed comparison to real materials, however, is lacking because the pristine Mott state is commonly obscured by antiferromagnetism and a complicated band structure. Here we study organic quantum spin liquids, prototype realizations of the single-band Hubbard model in the absence of magnetic order. Mapping the Hubbard bands by optical spectroscopy provides an absolute measure of the interaction strength and bandwidth—the crucial parameters that enter calculations. In this way, we advance beyond conventional temperature–pressure plots and quantitatively compose a generic phase diagram for all genuine Mott insulators based on the absolute strength of the electronic correlations. We also identify metallic quantum fluctuations as a precursor of the Mott insulator–metal transition, previously predicted but never observed. Our results suggest that all relevant phenomena in the phase diagram scale with the Coulomb repulsion *U*, which provides a direct link to unconventional superconductivity in cuprates and other strongly correlated materials.

The competition between the kinetic energy of the electrons—characterized by the bandwidth W—and their potential energy—determined by the Coulomb energy U—drives the Mott metal–insulator transition (MIT). Although this notion is widely accepted from the seminal works of Mott and Hubbard[1,2], the crossover from insulating to metallic has been discussed in a solely qualitative context in most cases, in particular not linking experimental results to the absolute scales available from state-of-the-art calculations[3,5]. Here we show that the relevant parameters that switch between localized and itinerant properties of the conduction electrons are the interaction strength and temperature normalized to the bandwidth, U/W and T/W.

As indicated in Fig. 1a, the Mott state, with a well-defined spectral gap, is delimited by a first-order transition at low temperatures and a crossover above the critical endpoint, which was recently identified as the quantum Widom line (QWL)[5] and provides interesting analogies to supercritical liquids and gases[6,7]. This physical picture emerges from the state-of-the-art dynamical mean-field theory (DMFT) description, which succeeds in capturing most salient features of the Mott point. The generic perspective, however, also reveals striking differences to conventional liquids, which usually form a solid on cooling or compression. Indeed, in classical solidification, the well-ordered crystal phase typically possesses a reduced entropy because the continuous rotational and translational symmetry that characterizes the liquid is spontaneously broken. The opposite behaviour, however, is observed for interacting electrons subject to Mott–Hubbard correlations, which is reminiscent of the paradigmatic Fermi liquid ^{3}He below $T = 0.3$ K: heating the fluid (under a pressure of about 3 MPa) transforms it into a solid. The peculiarity $\mathrm{d}p/\mathrm{d}T < 0$ of the melting curve is known as the Pomeranchuk effect, and the Clausius–Clapeyron relation implies that solid ^{3}He has a larger entropy than the liquid phase[8]. Likewise, the boundary to the Mott insulator exhibits a positive slope, $\mathrm{d}T_{\mathrm{MI}}/\mathrm{d}p > 0$, and the thermodynamic ground state is metallic. Here, the mobile electrons in the Fermi liquid state are predicted to have less entropy than those localized in the Mott state (Fig. 1b). This peculiar feature of electronic systems was never observed at low temperature, because it is commonly obscured by magnetic order (Fig. 1c). The recent discovery of a quantum spin liquid state in several organic Mott insulators[9–12] now provides us with the possibility to explore the paramagnetic insulating state down to $T = 0$. Such molecular conductors can be easily tuned through the phase transition by applying hydrostatic pressure or modifying the constituent molecules. With these possibilities at hand, elucidating the genuine Mott state in the low-temperature quantum regime becomes possible at last.

For our experimental investigation, we selected three well-characterized organic Mott insulators, β′-$EtMe_3Sb[Pd(dmit)_2]_2$ (EtMe) ($EtMe_3Sb$, ethyltrimethylstibonium; dmit, 1,3-dithiole-2-thione-4,5-dithiolate), κ-$(BEDT\text{-}TTF)_2Ag_2(CN)_3$ (AgCN) (BEDT-TTF, bis(ethylenedithio)tetrathiafulvalene)andκ-$(BEDT\text{-}TTF)_2Cu_2(CN)_3$ (CuCN). These compounds form a layered structure with dimers of organic molecules on a triangular lattice that carry one electron each (Fig. 2a–c), which results in half-filled, quasi-two-dimensional electronic systems well-described in terms of the single-band Hubbard model[13,14]. Optical investigations turn out to be the method

[1]Physikalisches Institut, Universität Stuttgart, Stuttgart, Germany. [2]Moscow Institute of Physics and Technology (State University), Dolgoprudny, Russia. [3]Institut za fiziku, Zagreb, Croatia. [4]Division of Materials Research, National Science Foundation, Arlington, VA, USA. [5]Materials Science Division, Argonne National Laboratory, Argonne, IL, USA. [6]Biomedizinische Chemie, Institut für Klinische Radiologie und Nuklearmedizin, Universität Heidelberg, Mannheim, Germany. [7]Faculty of Agriculture, Meijo University, Nagoya, Japan. [8]Division of Chemistry, Graduate School of Science, Kyoto University, Kyoto, Japan. [9]Toyota Physical and Chemical Research Institute, Nagakute, Japan. [10]Condensed Molecular Materials Laboratory, RIKEN, Wako-shi, Saitama, Japan. [11]Department of Physics and National High Magnetic Field Laboratory, Florida State University, Tallahassee, FL, USA. [12]Institut Néel – CNRS and Université Grenoble Alpes, Grenoble, France. *e-mail: andrej.pustogow@pi1.physik.uni-stuttgart.de

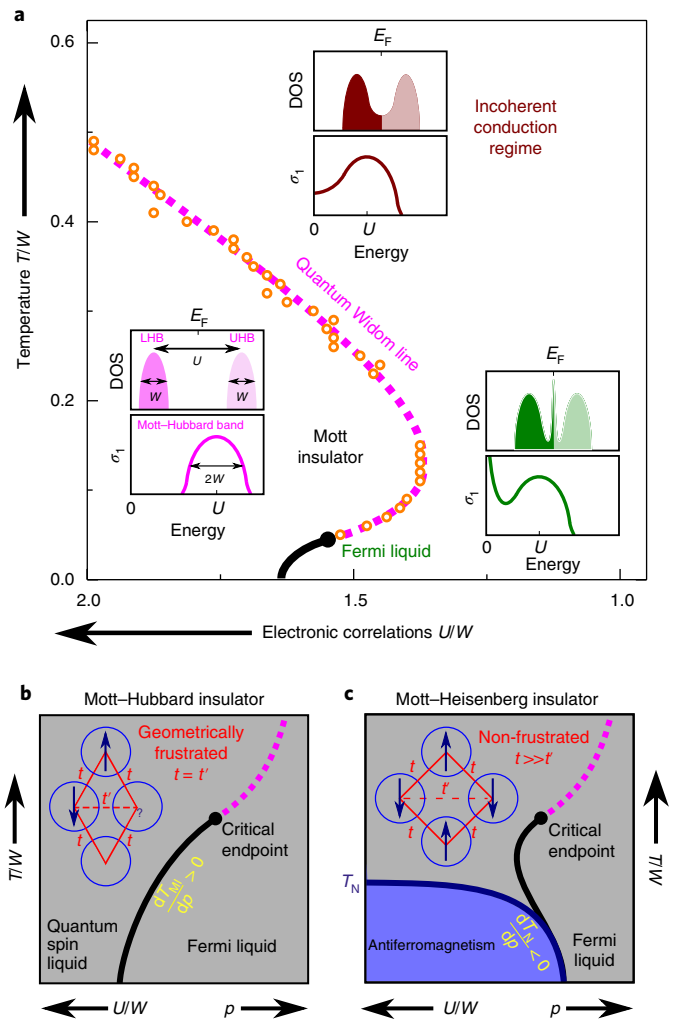

Fig. 1 | Theoretical phase diagram of the Mott insulator. a, The boundary of the Mott state with a gapped density of states (DOS) manifests as a first-order transition below the critical endpoint and as the quantum Widom line above. The orange circles correspond to DMFT calculations for different correlations U/W and temperatures T/W normalized to the bandwidth[5]. Although at high T the gap is filled by thermal excitations that cause incoherent transport over a broad U/W range, a quasiparticle peak develops at E_F as the hallmark of a Fermi liquid for $W > U \gg T$. Optical spectroscopy maps the DOS via transitions between the Hubbard bands and allows us to determine the Coulomb repulsion U and bandwidth W in the Mott state. **b**, At low T the magnetic ground state becomes significant for thermodynamics. In the absence of magnetic order (quantum spin liquid), the entropy remains large as $T \to 0$ ($S_{QSL} > S_{FL}$), which causes a positive slope of the phase transition due to the Clausius–Clapeyron relation. **c**, When geometrical frustration is relieved, antiferromagnetism stabilizes at low T. The ordered state has less entropy than the metallic phase, which implies $dT_N/dp < 0$. Figure reproduced from ref. [33].

of choice to study the corresponding correlation effects in these systems, because they can directly map the Mott–Hubbard excitations to give a quantitative measure of both the Coulomb repulsion U and the bandwidth W.

In Fig. 2a–c,e–g we plot the optical conductivity $\sigma_1(\omega)$ of EtMe, AgCN and CuCN single crystals probed at different temperatures. The most prominent feature is the Mott–Hubbard band centred at around 2,000 cm^{-1}, also observed in related materials[15]. This assignment is confirmed by DMFT calculations that employ the continuous-time quantum Monte Carlo (CTQMC) impurity solver, which reproduce the overall shape, asymmetry and intensity of the bands very well (Supplementary Information). The narrow peaks below 1,500 cm^{-1} correspond to vibrational features[16], which can be clearly separated from the overall change of the Mott–Hubbard band in the contour plots (Fig. 2e–g).

We determined U and W from the maximum and half-width, respectively, as indicated in Fig. 2d (see Fig. 1a). In a unified phase diagram, the three materials are quantitatively arranged in the order EtMe ($U/W = 2.35$), AgCN (1.96) and CuCN (1.52) on the descending horizontal U/W scale (Fig. 2h), consistent with ab initio density functional theory and extended Hückel calculations[11,17,18]. Although $U \approx 220$ meV is rather small in EtMe, the very narrow bandwidth $W \approx 90$ meV makes it the most-correlated electron system of this group. Compared to the κ-phase materials, the experimentally accessed temperatures (5–300 K) also cover a much broader vertical T/W range. This implies that the electronic compressibility is largest, and pressure has the strongest effect on U/W, consistent with experiment[19].

From Fig. 2a,d,e we notice that EtMe develops a well-defined Mott gap that continuously grows on cooling ($\Delta = 650$ cm^{-1} at 5 K). It opens at around 120 K, which coincides with the crossover temperature determined by pressure-dependent d.c. transport[19]. We thus provide conclusive experimental evidence that the QWL is, indeed, the true limitation of the Mott state associated with a spectral gap. The other two compounds do not exhibit a clear Mott gap due to a weaker correlation strength, that is, the Hubbard bands are broader with a larger overlap of the band tails.

We then looked for fingerprints of the ground state in the electrodynamic response at low frequencies (terahertz, far infrared), as these match the relevant energy scales in the problem, which are of the order of 100 K or less. The temperature evolution of the optical conductivity and the corresponding spectral weight (SW) well below ω_{max} (Fig. 3) reveals the insulating nature of the ground state of EtMe: the subgap absorption diminishes on cooling as the Mott gap opens. A similar but less pronounced freeze out of thermal excitations is observed for AgCN[20]. Most interesting, however, is the opposite behaviour of CuCN (Fig. 3a) with $\sigma_1(\omega)$ enhanced over a broad low-energy range (100–1,000 cm^{-1}) on lowering the temperature[21], which is typical for a metal but uncommon for an insulator. This is surprising given that no Drude peak, the hallmark of coherent transport, is present and that at zero frequency all the compounds—including CuCN—are electrical insulators as determined from d.c. transport (Fig. 3e).

This apparent contradiction is understood by the exceptional position of CuCN in the phase diagram: this compound is closer to the insulator–metal boundary than EtMe and AgCN (Fig. 2h), yet still on the insulating side. The Pomeranchuk-like back bending means that lowering the temperature effectively reduces the distance to the phase boundary, which drives the system towards the metallic state (Fig. 1b). We can therefore assign the strong non-thermal enhancement of the low-energy SW below $T = 70$ K (Fig. 3d), which coincides with the back-bending temperature of the QWL[19], to metallic quantum fluctuations in the Mott state that appear as a precursor of coherent transport on entering the coexistence region close to the MIT. This regime was predicted theoretically[5,22], but not observed previously. Only by scrutinizing quantum spin liquids we could circumvent magnetic order, which would otherwise conceal the actual low-energy behaviour—the less frustrated compound κ-(BEDT-TTF)$_2$Cu[N(CN)$_2$]Cl develops a hard gap in its antiferromagnetic state[21] despite being located even closer to the Mott MIT than CuCN[19]. From the trend of our data we suggest that the anomalous slope of the Mott MIT extends down to the lowest measured temperature. This is corroborated by the gradually decreasing transport gap of CuCN, which seemingly vanishes for $T \to 0$, consistent with a weakening of the insulating behaviour; in contrast, the transport gaps of EtMe and AgCN remain finite[23–25].

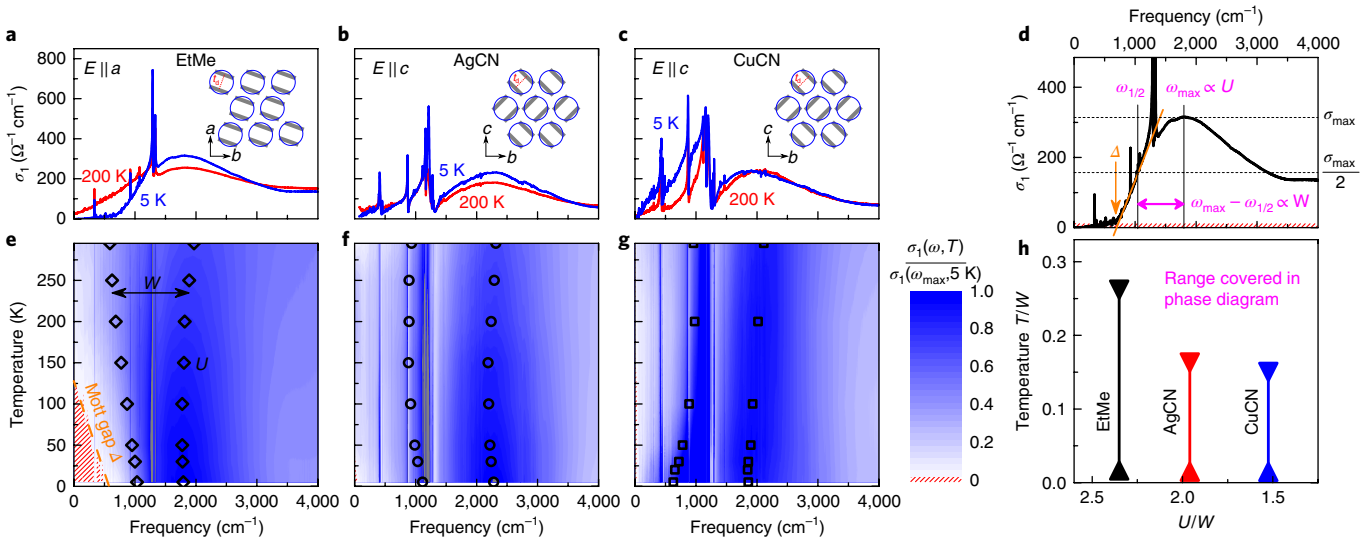

Fig. 2 | Temperature evolution of the optical conductivity of three QSL compounds. a–c, The dominant feature in EtMe (**a**), AgCN (**b**) and CuCN (**c**) that contains all the information of the intrinsic Mott physics is the Mott–Hubbard band centred at around 2,000 cm^{-1}. At low frequencies narrow phonon modes appear on top. **d**, The Coulomb repulsion U corresponds to the band maximum position ω_{max} and the half width at half maximum is proportional to the electronic bandwidth $W/\hbar = \omega_{max} - \omega_{1/2}$ (Fig. 1a). The bandgap Δ is determined by the linear extrapolation of the steepest slope. The red-shaded regions correspond to an optical conductivity smaller than the value at Δ. **e–g**, The contour plots for EtMe (**e**), AgCN (**f**) and CuCN (**g**) illustrate the temperature-dependent changes of the Mott–Hubbard band, where the open black symbols denote the maximum and half-maximum positions. The Mott gap of EtMe opens at around 120 K. **h**, The horizontal U/W and vertical T/W values (U and W extracted at 5 K, T = 5–300 K) determine the accessed region in the phase diagram. EtMe extends over the largest T/W range and correlations decrease from left to right via AgCN and CuCN . Figure reproduced from ref. [33].

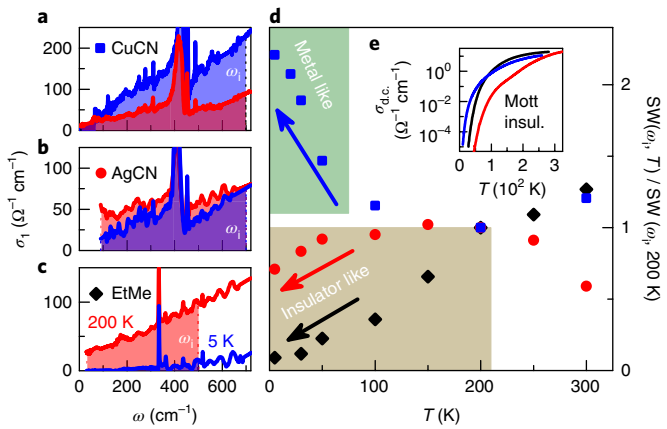

Fig. 3 | Correlation-dependent low-energy excitations. a–c, While the low-frequency conductivity is suppressed on cooling for EtMe (**c**) and AgCN (**b**), it increases for CuCN (**a**). **d**, The spectral weight SW (the integration range ω_1 is indicated by the shaded regions in **a–c**) summarizes the thermal evolution of the low-energy excitations. **e**, Although d.c. transport characterizes all the compounds as Mott insulators (insul.), CuCN exhibits a metal-like increase of the low-frequency SW that sets in below 70–80 K. Figure reproduced from ref. [33].

Numerous investigations have explored scaling relations at the critical endpoint of the Mott transition, and extracted critical exponents and certain universality classes[19,26–28]. Above the critical temperature the sharp phase boundaries dissolve into the QWL that arises from the interplay of U, W and T and separates between the Mott insulating state and an incoherent conduction regime. Pressure- and temperature-dependent transport studies give clear indications of this crossover[11,19], in full accord with theory[5]. Using the U/W and T/W scaling obtained from our optical studies, here we suggest a unified and quantitative phase diagram for all organic Mott insulators, as presented in Fig. 4 (Supplementary Information gives details). We are confident that the intrinsic properties of the Mott MIT should also prevail for spin-liquid compounds of different symmetry, for example kagome and other geometries. Investigations in this direction in other classes of materials are extremely compelling, but are not immediately straightforward due to the more complex band structures in candidate materials, such as the inorganic herbertsmithite[29].

When comparing our observations on the molecular Mott insulators to those obtained on transition metal compounds, it becomes clear that we now cover a range previously inaccessible, because the much larger energy scales that characterize these compounds push the first-order Mott MIT all the way up to room temperature[2] and the Widom line beyond the scales accessible in laboratory. For decades, V_2O_3 has served as the prime example of a Mott insulator because a slight Cr substitution allows a precise tuning from the paramagnetic metallic to the insulating phase by inverse chemical pressure[30]. Taking into account its large bandwidth of several electronvolts[31], this material fits well into our generic phase diagram (Fig. 4) and yet covers only a tiny part, as illustrated in the Supplementary Information.

Our present study of molecular quantum spin liquids provides a general picture of the Mott MIT as a whole, with the QWL as the organizing principle and quantum fluctuations that emerge already from the insulating side. We conclude that the organic compounds establish the proper standard for Mott physics, with direct implications for oxides. Recent DMFT studies infer that the Widom line formalism also applies to the pseudogap in cuprates[32], which encourages a similar rescaling approach for charge-carrier doping, as for the bandwidth-tuned Mott MIT presented here, which approaches the long-standing mystery of a high T_c.

The emerging scenario suggests an analogue classification on the metallic side that captures the bad metallic and Fermi-liquid

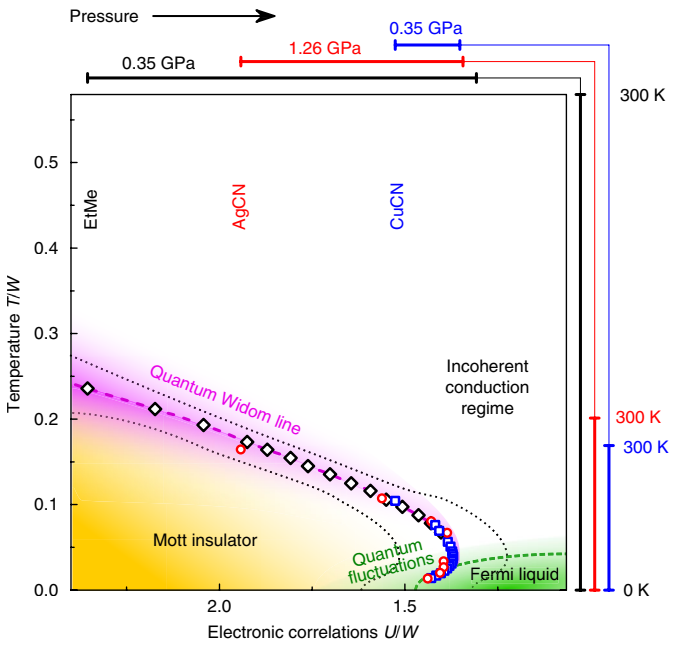

Fig. 4 | Quantitative phase diagram of pristine Mott insulators. The pressure-dependent transport data of EtMe, AgCN and CuCN acquired in other works[11,19] were rescaled on the basis of the parameters U and W extracted from our optical measurements. The vertical and horizontal bars indicate the investigated temperature and pressure ranges. All the data points collapse on a universal QWL on quantitative scales (the dotted black lines indicate the uncertainty of the QWL due to the experimental determination of U/W (Supplementary Information gives details), in excellent agreement with theory (Fig. 1a). The metallic-like T dependence of the low-frequency absorption of CuCN (Fig. 3) is a direct implication of its ambient pressure position ($U/W=1.52$) close to the metallic phase; on cooling, the material enters a regime of metallic quantum fluctuations that appears as a precursor of the Mott transition. Figure reproduced from ref. [33].

states, in which the effective mass renormalization m^*/m is linked to U/W on varying the interaction strength. Another delicate issue is the nature of the proposed coexistence region[3]: identifying the observed quantum fluctuations as spatially segregated metallic puddles implies that the effective mass does not diverge at the first-order Mott MIT, which clearly contrasts it to quantum critical systems. Moreover, with W and U as the only relevant quantities, it is a particularly intriguing question as to how spin excitations emerge on the insulating side as we are dealing here with spin-liquid compounds. The elaborated phase diagram provides a solid foundation to investigate systematically the spin degrees of freedom.

Methods

Methods, including statements of data availability and any associated accession codes and references, are available at https://doi.org/10.1038/s41563-018-0140-3.

Received: 10 August 2017; Accepted: 26 June 2018;
Published online: 06 August 2018

References

1. Gebhard, F. *The Mott Metal–Insulator Transition* (Springer, Berlin, 1997).
2. Imada, M., Fujimori, A. & Tokura, Y. Metal–insulator transitions. *Rev. Mod. Phys.* **70**, 1039–1263 (1998).
3. Vollhardt, D. Dynamical mean-field theory for correlated electrons. *Ann. Phys.* **524**, 1–19 (2012).
4. Keimer, B., Kivelson, S. A., Norman, M. R., Uchida, S. & Zaanen, J. From quantum matter to high-temperature superconductivity in copper oxides. *Nature* **518**, 179–186 (2015).
5. Vučičević, J., Terletska, H., Tanasković, D. & Dobrosavljević, V. Finite-temperature crossover and the quantum Widom line near the Mott transition. *Phys. Rev. B* **88**, 075143 (2013).
6. Xu, L. et al. Relation between the Widom line and the dynamic crossover in systems with a liquid–liquid phase transition. *Proc. Natl Acad. Sci. USA* **102**, 16558 (2005).
7. Simeoni., G. G. et al. The Widom line as the crossover between liquid-like and gas-like behaviour in supercritical fluids. *Nat. Phys.* **6**, 503–507 (2010).
8. Richardson, R. C. The Pomeranchuk effect. *Rev. Mod. Phys.* **69**, 683–690 (1997).
9. Shimizu, Y., Miyagawa, K., Kanoda, K., Maesato, M. & Saito, G. Spin liquid state in an organic Mott insulator with a triangular lattice. *Phys. Rev. Lett.* **91**, 107001 (2003).
10. Itou, T., Oyamada, A., Maegawa, S., Tamura, M. & Kato, R. Quantum spin liquid in the spin-1/2 triangular antiferromagnet $EtMe_3Sb[Pd(dmit)_2]_2$. *Phys. Rev. B* **77**, 104413 (2008).
11. Shimizu, Y. et al. Pressure-Tuned Exchange Coupling of a Quantum Spin Liquid in the Molecular Triangular Lattice κ–$(ET)_2Ag_2(CN)_3$. *Phys. Rev. Lett.* **117**, 107203 (2016).
12. Zhou, Y., Kanoda, K. & Ng, T.-K. Quantum spin liquid states. *Rev. Mod. Phys.* **89**, 025003 (2017).
13. Powell, B. J. & McKenzie, R. H. Quantum frustration in organic Mott insulators: from spin liquids to unconventional superconductors. *Rep. Prog. Phys.* **74**, 056501 (2011).
14. Hotta, C. Theories on frustrated electrons in two-dimensional organic solids. *Crystals* **2**, 1155–1200 (2012).
15. Faltermeier, D. et al. Bandwidth-controlled Mott transition in κ-(BEDT-TTF)$_2$Cu[N(CN)$_2$]Br$_x$Cl$_{1-x}$: optical studies of localized charge excitations. *Phys. Rev. B* **76**, 165113 (2007).
16. Dressel, M. et al. Lattice vibrations of the charge-transfer salt κ-(BEDT-TTF)$_2$Cu$_2$(CN)$_3$: comprehensive explanation of the electrodynamic response in a spin-liquid compound. *Phys. Rev. B* **93**, 081201 (2016).
17. Kandpal, H. C., Opahle, I., Zhang, Y.-Z., Jeschke, H. O. & Valentí, R. Revision of model parameters for κ-type charge transfer salts: an ab initio Study. *Phys. Rev. Lett.* **103**, 067004 (2009).
18. Kato, R. & Hengbo, C. Cation dependence of crystal structure and band parameters in a series of molecular conductors, β'-(Cation)$[Pd(dmit)_2]_2$ (dmit: 1,3-dithiole-2-thione-4,5-dithiolate). *Crystals* **2**, 861–874 (2012).
19. Furukawa, T., Miyagawa, K., Taniguchi, H., Kato, R. & Kanoda, K. Quantum criticality of Mott transition in organic materials. *Nat. Phys.* **11**, 221–224 (2015).
20. Nakamura, Y., Hiramatsu, T., Yoshida, Y., Saito, G. & Kishida, H. Optical properties of a quantum spin liquid candidate material, κ-(BEDT-TTF)$_2$Ag$_2$(CN)$_3$. *J. Phys. Soc. Jpn* **86**, 014710 (2017).
21. Kezsmarki, I. et al. Depressed charge gap in the triangular-lattice Mott insulator κ–$(ET)_2Cu_2(CN)_3$. *Phys. Rev. B* **74**, 201101 (2006).
22. Terletska, H., Vučičević, J., Tanasković, D. & Dobrosavljević, V. Quantum critical transport near the Mott transition. *Phys. Rev. Lett.* **107**, 026401 (2011).
23. Pinterić, M. et al. Anisotropic charge dynamics in the spin-liquid candidate κ-(BEDT-TTF)$_2$Cu$_2$(CN)$_3$. *Phys. Rev. B* **90**, 195139 (2014).
24. Pinteric, M. et al. Anions effects on the electronic structure and electrodynamic properties of the Mott insulator κ-(BEDT-TTF)$_2$Ag$_2$(CN)$_3$. *Phys. Rev. B* **94**, 161105 (2016).
25. Lazić, P. et al. Importance of van der Waals interactions and cation–anion coupling in an organic quantum spin liquid. *Phys. Rev. B* **97**, 245134 (2018).
26. Limelette, P. et al. Universality and critical behavior at the Mott transition. *Science* **302**, 89–92 (2003).
27. Kagawa, F., Miyagawa, K. & Kanoda, K. Unconventional critical behaviour in a quasi-two-dimensional organic conductor. *Nature* **436**, 534–537 (2005).
28. Gati, E. et al. Breakdown of Hooke's law of elasticity at the Mott critical endpoint in an organic conductor. *Sci. Adv.* **2**, e1601646 (2016).
29. Pustogow, A. et al. Nature of optical excitations in the frustrated kagome compound herbertsmithite. *Phys. Rev. B* **96**, 241114(R) (2017).
30. Hansmann, P. et al. Mott–Hubbard transition in V_2O_3 revisited. *Phys. Stat. Sol. B* **250**, 1251–1264 (2013).
31. Qazilbash, M. M. et al. Electrodynamics of the vanadium oxides VO_2 and V_2O_3. *Phys. Rev. B* **77**, 115121 (2008).
32. Sordi, G., Sémon, P., Haule, K. & Tremblay, A.-M. S. Pseudogap temperature as a Widom line in doped Mott insulators. *Sci. Rep.* **2**, 547 (2012).
33. Pustogow, A. *Unveiling Electronic Correlations in Layered Molecular Conductors by Optical Spectroscopy.* PhD Thesis, University of Stuttgart (2017).

Acknowledgements

We thank K. Kanoda and R. Valentí for fruitful discussions. Part of the work is supported by the Deutsche Forschungsgemeinschaft via DR228/41-1 and DR228/48-1. We also thank the Deutscher Akademischer Austauschdienst for support. This work was partially supported by JSPS KAKENHI grant no. JP16H06346. We acknowledge the Russian Ministry of Education and Science (Program '5 top 100'). We also acknowledge support from the Croatian Science Foundation project IP-2013-11-1011. J.A.S. acknowledges support from the Independent Research and Development program from the NSF while working at the Foundation and from the National High Magnetic Field Laboratory User Collaboration Grants Program. Work in Florida was supported by the NSF grant no. DMR-1410132, and the National High Magnetic Field Laboratory through the NSF cooperative agreement no. DMR-1157490 and the State of Florida. Parts of the text and results reported in this work are reproduced from the thesis of A.P.[33] at the University of Stuttgart, and accessible at https://doi.org/10.18419/opus-9487.

Author contributions

Most of the optical experiments and their analysis were conducted by A.P. with the help of M.B. The terahertz measurements were performed by E.Z. and B.G. Crystal growth and d.c. transport measurements on EtMe crystals were performed by R.K., and d.c. transport on AgCN and CuCN was measured by R.R. and A.L., respectively. The AgCN salts were grown by A.L., R.H., T.H., Y.Y. and G.S., and the CuCN crystals by A.L., R.H. and J.S. Theoretical calculations were carried out by T.-H.L. and V.D. in communication with S.F. The interpretation and draft of the manuscript were made by A.P. and M.D. who also conceived the project. All the authors contributed to the discussion and the final manuscript.

Competing interests

The authors declare no competing interests.

Additional information

Supplementary information is available for this paper at https://doi.org/10.1038/s41563-018-0140-3.

Reprints and permissions information is available at www.nature.com/reprints.

Correspondence and requests for materials should be addressed to A.P.

Publisher's note: Springer Nature remains neutral with regard to jurisdictional claims in published maps and institutional affiliations.

Methods

Materials. Plate-like organic single crystals were grown during several months by air oxidation in acetone (EtMe)[34,35] and electrochemical oxidation (AgCN and CuCN)[36,37] in RIKEN, Nagoya, Stuttgart and Argonne. The samples reach typical dimensions of $1\times1\times0.05\,mm^3$, $0.4\times0.3\times0.2\,mm^3$ and $1\times1\times0.2\,mm^3$ for EtMe, AgCN and CuCN, respectively. After selection and cleaning, the crystals were measured without further treatment; in particular, the optical reflectivity was probed on as-grown crystal surfaces.

Optical spectroscopy. Broadband optical spectra were recorded on various Fourier-transform infrared spectrometers equipped with the corresponding sources, beam splitters, polarizers, windows and detectors. The reflectivity was obtained by normalizing the signal of the sample to a gold mirror taking into account the tabulated frequency-dependent reflectivity of gold. To reach accurate absolute values and to account for diffraction effects in the far infrared ($\omega/2\pi c<700\,cm^{-1}$, where c is the speed of light in vacuum), we first measured the temperature-dependent sample reflection normalized to a big mirror, followed by evaporation of a thin gold layer (~300 nm in thickness) on the sample and, subsequently, a second measurement of the covered sample at the same temperatures. Eventually, the reflection was calculated by dividing the sample spectra without and with gold, both of which were normalized to a big mirror to account for the temporal fluctuations of the spectrometer. Typically, the low-frequency limit was 30–100 cm^{-1} depending on the crystal size. The frequency resolution was set to 1 cm^{-1}.

Several optical cryostats enabled us to cover the range $5\,K<T<300\,K$. Prior to cooling, the sample was aligned parallel to a gold mirror and the crystal axes were determined with an automated polarizer. Then, the cryostat was evacuated to minimize thermal contact to the surroundings and avoid the formation of ice on the sample. During cooling, the pressure in the sample chamber was typically 10^{-6}–10^{-5} mbar. The cooling rate was 1 K min^{-1}.

In addition to the Fourier-transform infrared reflection studies, temperature-dependent terahertz transmission was measured for EtMe and CuCN using coherent source (backward-wave oscillators) and pulsed time-domain spectrometers. Both spectrometers enabled us to calculate the real and imaginary parts of the conductivity $\sigma_1(\omega)+i\sigma_2(\omega)$ (i is imaginary unit) directly without using Kramers–Kronig relations[38,39]. Thus, we could measure the single crystals of EtMe and CuCN down to 6 cm^{-1}; the low-frequency limit for AgCN was around 100 cm^{-1} due to the small crystal size. For all the compounds, the reflectivity was measured up to the visible (20,000 cm^{-1}) by Fourier transform spectroscopy. In addition, we determined the room temperature reflectivity of EtMe up to 45,000 cm^{-1} by ellipsometric techniques.

Data processing. To calculate the frequency-dependent conductivity by the Kramers–Kronig relations, the optical reflectivity obtained by the various methods and spectrometers was merged (reflectivity data are shown in the Supplementary Information and Supplementary Figs. 3 and 4). In rare cases, it was required to slightly shift the raw data (several percent of mismatch can occur due to alignment in the different set-ups). Then, the low- and high-frequency reflectivities were extrapolated to 0.001 and $10^6\,cm^{-1}$, respectively. While generalized Hagen–Rubens behaviour ($R=a-b\omega^n$, where $a<1$ and $0<n<0.5$) was extrapolated at low frequencies, a ω^{-4} decay was applied towards high frequencies. For EtMe and CuCN, the low-frequency optical conductivity that resulted from the Kramers–Kronig calculation was replaced by the terahertz data. Most importantly, the optical conductivity discussed here is not affected by the extrapolation.

Electrical transport. The temperature-dependent resistivity was determined within the conducting plane utilizing the standard four-point method[23,24,40]. A current of typically 10 μA was applied to avoid heating of the sample. Electrical contacts were realized by 25 μm gold wires attached to the crystal by conductive carbon paste. The specimens were mounted on a sapphire plate for a good thermal contact. Utilizing a ^{4}He exchange gas cryostat, the cooling rate was adjusted to approximately 0.1 K min^{-1} down to 2 K to ensure thermal equilibrium, to prevent cracking and to minimize disorder effects.

Pressure-dependent experiments on CuCN (Supplementary Fig. 13b,c) were performed in a CuBe oil pressure cell. The pressure was corrected for the temperature-dependent freezing of the medium.

In Fig. 4 and Supplementary Fig. 1, we incorporated published data of the pressure- and temperature-dependent resistivity measurements[11,19] on EtMe, AgCN and CuCN. The inflection points of the resistivity versus pressure are taken as a crossing of the QWL at certain temperatures. This agrees well with the determination from our temperature-dependent transport studies presented in Supplementary Figs. 2 and 13c.

DMFT calculations. DMFT[41] calculations were performed using a single-band Hubbard model at half-filling, and assuming a simple semicircular density of states. We used the state-of-the-art CTQMC quantum impurity solver, as implemented by Haule[42]. The number of Monte Carlo steps was set to 1×10^9 for precise sampling. In the insulating phase, the convergence was checked by requiring the local Green's function to satisfy the self-consistent criterion, $|G^{i+1}(i\omega_0)-G^i(i\omega_0)|\approx10^{-4}$. This was typically achieved within 20 iterations, where i represents the iterations and $\omega_0=\pi T$. We performed analytical continuation on the Matsubara frequency Green's function using maximum entropy methods[43]. Then, the self-energy was calculated from the DMFT self-consistent condition:

$$\Sigma(\omega)=\omega+\mu-G^{-1}(\omega)-t^2G(\omega) \tag{1}$$

We set the half-bandwidth $D=\frac{1}{2}W_0=1$ as our energy unit. With the obtained self-energy, we calculate the optical conductivity using the Kubo formula:[41]

$$\sigma(\omega)=\sigma_0\int\int d\varepsilon d\nu\Phi(\varepsilon)A(\varepsilon,\nu)A(\varepsilon,\nu+\omega)\frac{f(\nu)-f(\nu+\omega)}{\omega} \tag{2}$$

where $A(\varepsilon,\nu)=-(1/\pi)\mathrm{Im}(\varepsilon+\mu-\nu-\Sigma(\varepsilon))^{-1}$ is the momentum and frequency dependent spectral function, where the momentum dependence enters through the band structure dispersion $\varepsilon(k)$, f is the Fermi function, $\Phi(\varepsilon)=\Phi(0)[1-(\varepsilon/D)^2]^{3/2}$ and $\sigma_0=2\pi e^2/\hbar$ is the conductance quantum. Here we set $\sigma_{IRM}=e^2\Phi(0)/\hbar D$ as our conductivity unit, where σ_{IRM} is the Ioffe–Regel–Mott limit to distinguish the metal and bad metallic behaviour. The obtained spectra, shown in the Supplementary Fig. 12, resemble very well our experimental data plotted in Fig. 2.

To evaluate the QWL, the DMFT calculation was performed on the triangular lattice to compare with the organic compounds in this report. To obtain a reliable QWL, the iterated perturbation theory was applied as our impurity solver (Fig. 1a), which has been shown to have accurate results compared to numerically exact CTQMC but to suffer from less numeric error, especially in triangular lattice systems. We employed the λ analysis to locate the QWL[5,22], in which λ corresponds to the curvature of the free energy functional and shows a minimum at the QWL. More specifically, λ can be obtained from the iterative solution of DMFT equations[5,22]:

$$\delta G^{(n+1)}(i\omega_n)-\delta G^{(n)}(i\omega_n)=e^{-n\lambda}\delta G^{(0)}(i\omega_n) \tag{3}$$

where $\delta G^{(n)}=G^{(n)}-G_{DMFT}$ and G_{DMFT} is the converged DMFT Green's function. Therefore, λ corresponds to the convergence rate towards the DMFT solution.

Data availability. The authors declare that the data supporting the findings of this study are available within the paper and its Supplementary Information. For further details, contact A.P. or M.D.

References

34. Kato, R., Fukunaga, T., Yamamoto, H. M., Ueda, K. & Hengbo, C. Crystal structure and band parameters of mixed crystals derived from quantum spin liquid β′-$EtMe_3Sb[Pd(dmit)_2]_2$ (dmit: 1,3-dithiole-2-thione-4,5-dithiolate). *Phys. Stat. Solidi B* **249**, 999–1003 (2012).
35. Kato, R. Development of pi-Electron Systems Based on [M(dmit)$_2$] (M = Ni and Pd; dmit: 1,3-dithiole-2-thione-4,5-dithiolate) Anion Radicals. *Bull. Chem. Soc. Jpn* **87**, 355–374 (2014).
36. Geiser, U. et al. Superconductivity at 2.8 K and 1.5 kbar in κ-$(BEDT\text{-}TTF)_2Cu_2(CN)_3$: the first organic superconductor containing a polymeric copper cyanide anion. *Inorg. Chem.* **30**, 2586 (1991).
37. Hiramatsu, T. et al. Design and preparation of a quantum spin liquid candidate κ-$(ET)_2Ag_2(CN)_3$ having a nearby superconductivity. *Bull. Chem. Soc. Jpn* **90**, 1073–1082 (2017).
38. Dressel, M. & Grüner, G. *Electrodynamics of Solids* (Cambridge Univ. Press, Cambridge, 2002).
39. Gorshunov, B. P. et al. Terahertz BWO-spectroscopy. *Int. J. Infrared Millim. Waves* **26**, 1217–1240 (2005).
40. Yasin, S. et al. Transport studies at the Mott transition of the two-dimensional organic metal κ-$(BEDT\text{-}TTF)_2Cu[N(CN)_2]Br_xCl_{1-x}$. *Eur. Phys. J. B* **79**, 383–390 (2011).
41. Georges, A., Kotliar, G., Krauth, W. & Rozenberg, M. J. Dynamical mean-field theory of strongly correlated fermion systems and the limit of infinite dimensions. *Rev. Mod. Phys.* **68**, 13–125 (1996).
42. Haule, K. Quantum Monte Carlo impurity solver for cluster dynamical mean-field theory and electronic structure calculations with adjustable cluster base. *Phys. Rev. B* **75**, 155113 (2007).
43. Jarrell, M. & Gubernatis, J. E. Bayesian inference and the analytic continuation of imaginary-time quantum Monte Carlo data. *Phys. Rep.* **269**, 133–195 (1996).